Modeling Commercial-Scale CO_2 Storage in the Gas Hydrate Stability Zone with PFLOTRAN v6.0

Michael Nole[1], Jonah Bartrand[1], Fawz Naim[2], and Glenn Hammond[1]

[1]Pacific Northwest National Laboratory, Richland, 99354, USA
5   [2]Ohio State University, Columbus, 43210, USA

Correspondence to: Michael Nole (michael.nole@pnnl.gov)

Abstract

Safe and secure carbon dioxide (CO_2) storage is likely to be critical for mitigating some of the most dangerous effects of climate change. In the last decade, there has been a significant increase in activity associated with reservoir characterization
10   and site selection for large-scale CO_2 storage projects across the globe. These prospective storage sites tend to be ~~terrestrial sites~~ selected for their optimal structural, petrophysical, and geochemical trapping potential. However, it has also been suggested that storing CO_2 in reservoirs within the ~~gas~~ CO_2 hydrate stability zone (GHSZ), characterized by high pressures and low temperatures (e.g., Arctic or marine environments), could provide natural thermodynamic and solubility barriers to gas leakage. Evaluating the prospect of commercial-scale, long-term storage of CO_2 in the GHSZ requires reservoir-scale
15   modelling capabilities designed to account for the unique physics and thermodynamics associated with these systems. We have developed the HYDRATE flow mode and accompanying fully implicit parallel well model in the massively parallel subsurface flow and reactive transport simulator PFLOTRAN to model CO_2 injection into the marine GHSZ. We have applied these capabilities to a set of CO_2 injection scenarios designed to reveal the challenges and opportunities for commercial-scale CO_2 storage in the GHSZ.

20   ## 1 Introduction

Large-scale deployment of carbon capture and storage (CCS) projects is likely to be critical for constraining future global temperature increase due to climate change, yet major uncertainties exist regarding potential injectivity of CO_2 in subsurface reservoirs (Lane et al., 2021). Evaluating ~~terrestrial~~ CO_2 storage sites for long-term sequestration requires synthesizing sophisticated laboratory, field, and modelling tools to assess the CO_2 trapping potential of a prospective subsurface reservoir
25   during a large-scale injection over a significant post-injection performance period. CO_2 trapping in ~~terrestrial~~ sequestration applications involves potentially both physical and chemical trapping mechanisms which include structural, solubility, capillary, and mineralization trapping (Al Hameli et al., 2022). Currently, large-scale carbon capture and storage (CCS) projects around the globe are each storing over 400,000 metric tons (Mt) of CO_2 annually (Snæbjörnsdóttir et al., 2020); the U.S. Department of Energy's CarbonSAFE initiative aims to develop CO_2 storage complexes across the U.S. that would be

30   capable of storing total volumes exceeding 50 million metric tons (MMt) of CO_2 each (Sullivan et al., 2020). To achieve this vision, a diverse set of potential reservoir host rocks and environments is being considered. This includes speculation about the feasibility of offshore CO_2 sequestration and mineralization, such as in Cascadia Basin basalts offshore the U.S. Pacific Northwest (Goldberg et al., 2018). Shallow sub-sea environments are not only isolated from the atmosphere by a large water body, but they can also exist in a unique pressure and temperature regime conducive for forming gas hydrate.

35

    Gas hydrate is a solid-phase, non-stoichiometric mixture of low molecular weight gas molecules occupying free spaces in a solid water lattice. Hydrates of several different gases occur abundantly in nature, but since the hydrate phase is only stable at high pressures and low temperatures it is only found naturally on Earth in the pore space of soils in either permafrost or sub-sea environments. ~~Methane~~ CH_4 hydrate is of interest for its potential as a natural gas energy resource (Collett, 2000; Oyama

40 et al., 2017; Singh et al., 2022), for its potential role in global carbon cycling as the climate changes (Ruppel and Kessler, 2017), and for its role as a geohazard (Zander et al., 2018; Kaminski et al., 2020). On the other hand, ~~carbon dioxide (CO_2)~~ hydrate, which ~~forms~~ can form at similar pressures and temperatures as CH_4~~methane~~ hydrate, is increasingly being explored as a potential means to permanently sequester CO_2 as a climate change mitigation solution that comes with additional safety factors beyond those typically encountered in ~~terrestrial~~ more conventional CO_2 sequestration scenarios. These include the fact

45 that CO_2 hydrate~~it~~ is immobile in sediment pore space, which adds a thermodynamic barrier to gas escape, and the ability of the ocean to dissolve leaked CO_2~~presence of a significant ocean sink~~ in marine environments which isolates CO_2 from release into the atmosphere (Tohidi et al., 2010). An added benefit of CO_2 injection into the CH_4~~methane~~ hydrate stability zone is that CO_2 hydrate ~~is typically~~can be more thermodynamically favourable than CH_4~~methane~~ hydrate, meaning it could theoretically be possible to use CO_2 to ~~kick out~~replace CH_4~~methane~~ ~~from~~ in the hydrate phase, thus sequestering CO_2 while producing

50 natural gas from a CH_4~~methane~~ hydrate deposit (Koh et al., 2016).

    CO_2 sequestration in gas hydrate form can only occur in a finite bounded temperature and pressure range. In terms of a soil column, there exists a depth-bounded gas hydrate stability zone (GHSZ) in the subsurface in which CO_2 hydrate can form. In a marine environment, the CO_2 GHSZ typically begins several meters above the seafloor, but hydrate does not form freely in

55 the water column (except for, e.g., as a gas bubble crust [Fu et al., 2021]) because the guest molecule gas (e.g., CO_2) typically cannot become concentrated enough in the water to do so. Therefore, the seafloor is typically the shallowest extent of hydrate formation in marine systems. ~~Relative to deeper sediments, this point usually represents a minimum temperature and pressure.~~ Working downward through the GHSZ, pressure increases roughly hydrostatically and temperature increases along a geothermal gradient. Increases in pressure stabilize hydrate, while increases in temperature destabilize hydrate. The geothermal

60 temperature change effect on hydrate stability outweighs the hydrostatic pressure change effect, so there exists a depth below the seafloor where the temperature is too high to form hydrate, known as the base of the gas hydrate stability zone (BHSZ). Overall, the specific thickness of the bulk GHSZ is dependent on pressure, temperature, porewater salinity and gas composition (Sloan and Koh, 2007).

65 For a potential host reservoir within the CO$_2$ GHSZ, the long-term CO$_2$ storage potential of the reservoir would consider the thermodynamic trapping mechanism of solid gas hydrate formation in addition to traditional trapping mechanisms. Several experimental studies have demonstrated the process of CO$_2$ trapping and hydrate conversion in the CO$_2$ GHSZ at the lab-scale, ~~demonstrating~~ showing how conversion of CO$_2$ into a solid phase adds an additional safety factor (Gauteplass et al., 2020; Rehman et al., 2021). An experimental study of layered sediments using different injection strategies demonstrated the need

70 to consider thermal management when designing a CO$_2$ injection in the GHSZ and suggested multilateral perforated horizontal wells may achieve the most optimal CO$_2$ conversion efficiency (Pang et al., 2024). However, reservoir-scale modelling studies of the transport and thermodynamic phenomena associated with injection of CO$_2$ in commercial volumes into the GHSZ are lacking.

75 We present several new capabilities developed in the open source, massively parallel multiphase flow and reactive transport simulator PFLOTRAN (Hammond et al., 2014) to model reservoir-scale injection of CO$_2$ in the CO$_2$ GHSZ. We have extended PFLOTRAN's HYDRATE mode capabilities to model free-phase CO$_2$ flow properties and CO$_2$ hydrate phase behaviour. Additionally, we introduce a fully coupled parallel well model that can be used to model CO$_2$ injection into heterogeneous media and can adapt to changes in flow properties associated with hydrate formation in the vicinity of the wellbore. Finally,

80 we add a new fully coupled salt mass balance to consider salinity and salt precipitation effects in the GHSZ. We demonstrate these capabilities on a series of test problems designed to elucidate the challenges and opportunities associated with commercial-scale injection of CO$_2$ into the GHSZ.

2 Methods

 PFLOTRAN's HYDRATE mode was originally developed to model ~~methane~~CH$_4$ generation, transport, and structure 1 (SI)

85 gas hydrate formation in deep marine and Arctic terrestrial reservoirs. PFLOTRAN's HYDRATE mode has been benchmarked against other reservoir simulators for modelling ~~methane~~CH$_4$ gas production from hydrate reservoirs (White et al., 2020). It has been used to predict shallow gas generation and gas hydrate formation offshore the eastern U.S. (Eymold et al., 2021), to study relationships between gas generation and slope stability along the U.S. Atlantic margin (Carty and Daigle, 2022), and to model gas hydrate accumulation offshore Norway (Frederick et al., 2021). An extension of HYDRATE mode to include

90 salinity coupling was developed to investigate viscous fingering and convective mixing in layered marine sediments during ~~methane~~CH$_4$ hydrate formation over geologic time (Fukuyama et al., 2023). Here, we have redeveloped PFLOTRAN's HYDRATE mode to optionally consider CO$_2$ as the working gas; to couple fully implicitly with a new parallel well model; to include a new fully coupled salt mass balance; and to consider variable salinity effects on H$_2$O-CO$_2$-NaCl mixtures and the CO$_2$ hydrate phase boundary.

2.1 Governing Equations

A system of three mass balance equations, one energy balance, and one well equation is now solved fully implicitly in PFLOTRAN's HYDRATE mode. The mass conservation equations take the following form:

$$\frac{\partial}{\partial t}\phi \sum_{\alpha=\text{l,g,h,i,s}}\left(s_\alpha \rho_\alpha x_j^\alpha\right) + \nabla \cdot \left(\boldsymbol{q}_\text{l}\rho_\text{l}x_j^\text{l} + \boldsymbol{q}_\text{g}\rho_\text{g}x_j^\text{g} - \phi s_\text{l}D_\text{l}\rho_\text{l}\nabla x_j^\text{l} - \phi s_\text{g}D_\text{g}\rho_\text{g}\nabla x_j^\text{g}\right) = Q_j + Q_{\text{w},j} \,, \tag{1}$$

where phase α can be liquid (l), gas (g), hydrate (h), ice (i), or salt precipitate (s); component j includes water, gas (CO_2, CH_4, or air), and salt (NaCl); s_α is the saturation of phase α; ρ_α is the density of phase α; x_j^α is the mole fraction of component j in phase α; q_l is the liquid Darcy flux vector; q_g is the gas Darcy flux vector; D_l is the liquid phase diffusivity; D_g is the gas phase diffusivity; ϕ is the porosity; and Q_j includes any non-well sources/sinks of component j; and $Q_{\text{w},j}$ is a source/sink of component j from a well. Solid phases are considered immobile and include the hydrate, ice, and salt precipitate phases. Mole fractions of components in the solid phases are fixed: by the hydration number in the hydrate phase, as pure water in the ice phase, and as pure salt in the salt precipitate phase. Formation of gas hydrate and ice therefore results in salt exclusion and aqueous dissolved salinity enhancement, which affects the hydrate phase boundary and gas solubility in the brine.

The energy conservation equation takes the form:

$$\sum_{\alpha=\text{l,g,h,i,s}}\left(\frac{\partial}{\partial t}(\phi s_\alpha \rho_\alpha U_\alpha) + \nabla \cdot (\boldsymbol{q}_\alpha \rho_\alpha H_\alpha)\right) + \frac{\partial}{\partial t}\left((1-\phi)\rho_\text{r}C_p T\right) - \nabla \cdot (\kappa \nabla \text{T}) = Q_e + Q_{\text{w},e} \,, \tag{2}$$

where U_α is the internal energy of phase α, H_α is the enthalpy of phase α, ρ_r is the rock density, C_p is the heat capacity of the rock, κ is the composite thermal conductivity of the medium, T is the temperature, Q_e includes any non-well heat sources/sinks, and $Q_{\text{w},e}$ is a heat source/sink imposed by the well (e.g., a heater in addition to a fluid injection). Exothermic hydrate formation (and vice versa, i.e., endothermic hydrate dissociation) is captured here by a decrease in internal energy of the hydrate phase during formation; this typically results in either an increase in system temperature or a change in phase saturations in three-phase systems. As we will show later, this phenomenon is important during CO_2 injection in the short term and it can continue to buffer conversion between phases for hundreds of years; similar effects have been shown for natural CH_4 hydrate systems where the base of the gas hydrate stability zone is shifted due to climactic changes (Owulunmi et al., 2022).

2.2 Well Model

125 A fully implicit, parallel well model has also been incorporated into HYDRATE mode. A well model can more accurately represent the insertion of a (comparably) small cylindrical wellbore into a reservoir grid cell than a standard source/sink term. Given a prescribed surface injection rate of CO_2 into the well, the well model solves for pressure variation along a wellbore and dynamically adjusts flow rates into the reservoir in response to changes in reservoir physical properties like permeability. This phenomenon can be critical to capture in a horizontal well or injection into a heterogeneous reservoir in the gas hydrate

130 stability zone, where near-wellbore formation (or dissociation) of gas hydrate can significantly alter reservoir permeability and thus injection behaviour. The well model developed for HYDRATE mode is a hydrostatic well model based off the design of White et al. (2013) but with key modifications including full parallelization to run flexibly on very large, unstructured grids and the addition of a thermal component; as we show here, injection temperature could be one of the most important design considerations for CO_2 storage in the gas hydrate stability zone. The well model developed here accounts for the enthalpy of

135 the injected CO_2 at the prescribed temperature and wellbore pressure using the same equation of state (EOS) as the reservoir.

Solving a hydrostatic well model involves solving one extra conservation equation per well in addition to the reservoir mass and energy conservation equations. PFLOTRAN uses a fully implicit Newton-Raphson nonlinear solution search method; for each distinct well, ~~This means that for one well, only~~only one extra row and one extra column ~~are used in the fully implicit~~

140 ~~flow~~are added to the Jacobian~~, not an extra row and extra column for each reservoir cell associated with a well~~. For each reservoir cell intersected by a well, well pressure is computed at the centroid of the well section crossing through the reservoir. All well pressures are determined from the bottom-hole pressure, a primary variable (see Section 2.~~3~~4). The well model conservation equation is compact and reads as follows:

145 $$\sum_i Q_{w,j}^i = q_{w,j} \,, \tag{3}$$

where i is the discrete reservoir cell index through which the wellbore passes, $Q^i_{w,j}$ are the reservoir source/sink terms of phase j associated with a well in reservoir grid cell i, and $q_{w,j}$ is the prescribed surface injection rate of phase j.

150 Well flux at each reservoir grid cell is computed as a function of the pressure difference between the well and the reservoir cell (free phase CO_2 pressure for gas injection) scaled by the well index as follows:

$$Q_{w,j} = -\frac{WI\rho_j}{\mu_j}(P_w - (P_r + \rho_j \boldsymbol{g}\Delta z_{w-r})) \tag{4}$$

where P_w is the well node pressure, P_r is the reservoir pressure of phase j in the grid cell associated with a given well node, and Δz_{w-r} is the vertical distance between well node centre and reservoir cell centre. The well can be oriented in any direction in 3D. To account for permeability anisotropy and arbitrary well orientations, the well index, WI, is calculated using a 3D extension of the Peaceman equation (White et al., 2013):

$$WI = \sqrt{WI_x^2 + WI_y^2 + WI_z^2} \tag{5}$$

$$WI_x = \frac{2\pi\sqrt{k_y k_z}L_x}{\ln\left(\frac{r_{0,x}}{r_w}\right)+s} \; ; \; WI_y = \frac{2\pi\sqrt{k_x k_z}L_y}{\ln\left(\frac{r_{0,y}}{r_w}\right)+s} \; ; \; WI_z = \frac{2\pi\sqrt{k_x k_y}L_z}{\ln\left(\frac{r_{0,z}}{r_w}\right)+s} \tag{6}$$

$$r_{0,x} = 0.28 \frac{\left(\left(\frac{k_y}{k_z}\right)^{0.5}\Delta z^2 + \left(\frac{k_z}{k_y}\right)^{0.5}\Delta y^2\right)^{0.5}}{\left(\frac{k_y}{k_z}\right)^{0.25}+\left(\frac{k_z}{k_y}\right)^{0.25}} \; ; \; r_{0,y} = 0.28 \frac{\left(\left(\frac{k_x}{k_z}\right)^{0.5}\Delta z^2 + \left(\frac{k_z}{k_x}\right)^{0.5}\Delta x^2\right)^{0.5}}{\left(\frac{k_x}{k_z}\right)^{0.25}+\left(\frac{k_z}{k_x}\right)^{0.25}} \; ; \; r_{0,z} = 0.28 \frac{\left(\left(\frac{k_x}{k_y}\right)^{0.5}\Delta y^2 + \left(\frac{k_y}{k_x}\right)^{0.5}\Delta x^2\right)^{0.5}}{\left(\frac{k_x}{k_y}\right)^{0.25}+\left(\frac{k_y}{k_x}\right)^{0.25}} \tag{7}$$

where s is the well skin, r_w is the wellbore radius, WI_α are well indices, k_α are the absolute permeabilities of the medium, L_α are the projections of each well leg, and $r_{0,\alpha}$ are the Peaceman radii in each principal direction $\alpha \in \{x, y, z\}$.

The bottomhole pressure of the well is solved as a primary variable as part of a fully coupled system of equations (Section 2.4). Pressures of each well segment are then directly calculated as functions of the bottomhole pressure by a hydrostatic adjustment to the depth of each well segment centre, where the density of the gas phase is updated as a function of pressure and injection temperature.

2.3 Constitutive Relationships

Diffusive flux is modelled using Fick's Law with diffusivities computed as functions of temperature and salinity for CO_2 (Cadogan et al., 2014) and NaCl (Reid et al., 1987). Advective fluxes of mobile phases are computed by employing a two-phase Darcy's Equation:

$$q_\alpha = -\frac{k k_\alpha^r}{\mu_\alpha}\nabla(P_\alpha - \rho_\alpha \boldsymbol{g}z) \tag{4}$$

where k is the intrinsic permeability of the medium, k_α^r is the relative permeability of phase α, μ_α is the viscosity of phase α, P_α is the pressure of phase α, $\boldsymbol{g}$ is the gravity vector, and z is depth. Relative permeability is computed as a function of phase saturations according to one of a suite of standard relative permeability relationships available in PFLOTRAN. Phase densities and viscosities are computed as functions of temperature, pressure, and salinity according to several options in PFLOTRAN (e.g., the Span-Wagner equation of state for CO_2, IF97 equation

of state ~~is typically used~~for water). Salt (NaCl) ~~is tracked only in the aqueous phase~~mass can be distributed in either the aqueous or solid salt precipitate phases, and aqueous dissolved salt mass affects brine flow properties like density (Haas, 1976), viscosity (Phillips et a., 1981), enthalpy, and diffusivity (Cadogan et al., 2014; Belgodere et al., 2015).

Gas phase pressure and liquid phase pressure are related as a function of gas phase saturation through a choice of capillary pressure functions available in PFLOTRAN. When the gas hydrate phase is present, a capillary pressure associated with the hydrate phase is computed using the same capillary pressure function as the gas phase, scaled by the ratio of interfacial tension vis-à-vis Leverett scaling (Leverett, 1941). This capillary pressure is used in the Gibbs-Thomson equation vis-à-vis the Young-Laplace equation to determine the hydrate 3-phase equilibrium temperature depression required to precipitate hydrate in pores as follows:

$$\Delta T_{\mathrm{m}} = -\frac{T_{\mathrm{mb}} P_{\mathrm{c}}}{\Delta H_{\mathrm{m}} \rho_{\mathrm{h}}} \tag{$\cancel{5}$9}$$

where ΔT_{m} is the change in the hydrate melting temperature, P_{c} is the hydrate phase capillary pressure, T_{mb} is the bulk melting temperature, ΔH_{m} is the specific enthalpy of the phase transition, and ρ_{h} is the density of solid hydrate. A similar method is often used to compute ice freezing temperature depression vis-à-vis the Clausius-Clapeyron equation. This effect is typically only significant in fine-grained sediments and/or at very high effective hydrate phase saturations (Anderson et al., 2003).

When both gas hydrate and free gas occupy significant fractions of the pore space, as would be common during CO_2 injection, their combined presence in the pore system should be accounted for through an effective saturation that is passed to the capillary pressure function. At three-phase (aqueous, free gas/CO_2 phase, gas hydrate) equilibrium, the chemical potential of CO_2 in the gas hydrate phase at a given hydrate capillary pressure must equal that of CO_2 in the free gas phase at a different free gas capillary pressure and dissolved CO_2. At bulk thermodynamic equilibrium, free gas and gas hydrate are stable together at a single pressure and temperature. In porous media, capillary effects on both the hydrate phase and gas phase lead to a window of possible pressures and temperatures over which three-phase equilibrium can be maintained (Clennell et al., 1999). To incorporate this effect and maintain thermodynamic reversibility, we adopt the approach of Liu and Flemings (2011) and require free gas and gas hydrate to partition the large pore space equally when both are present (Nole et al., 2018). This partitioning scheme results in the following effective saturations of free gas and gas hydrate:

$$s_{\alpha,\mathrm{eff}} = \begin{array}{ll} 2s_{\alpha}, & s_{\alpha} < s_{\beta} \\ s_{\alpha} + s_{\beta}, & \text{otherwise} \end{array} \tag{$\cancel{6}$10}$$

where $s_{\alpha,\mathrm{eff}}$ is the effective saturation of nonwetting phase α and β is the other nonwetting phase in a 3-phase system where liquid water is the wetting phase.

~~Well flux at each reservoir grid cell is computed as a function of the pressure difference between the well and the reservoir~~
~~cell (free gas [CO₂] phase pressure for gas injection) scaled by the well index as follows:~~

$$\cancel{Q_{w,j} = \frac{WI\rho_j}{\mu_j}(P_w - (P_r + \rho_j g \Delta z_{w-r}))} \tag{7}$$

~~where P_w is the well node pressure, P_r is the reservoir pressure of phase j in the grid cell associated with a given well node,~~
~~and Δz_{w-r} is the vertical distance between well node centre and reservoir cell centre. The well index, WI, is calculated using a~~
~~3D extension of the Peaceman equation incorporating wellbore radius, well skin factor, reservoir directional permeability, and~~
~~reservoir grid discretization (White et al., 2013).~~

The presence of gas hydrate in the pore space of a reservoir decreases the reservoir's permeability below its intrinsic (water-saturated) permeability. We model permeability reduction as a function of hydrate saturation as follows (Dai and Seol, 2014):

$$k_{\text{eff}} = \frac{(1-s_h)^3}{(1+2s_h)^2} \tag{$\cancel{8}11$}$$

where k_{eff} is the effective permeability coefficient and is multiplied by intrinsic permeability to compute the effective absolute permeability.

Heat transfer occurs through mobile fluid phase flow, phase transitions, thermal conduction, and injection/production. Fluid phase enthalpies are computed using corresponding equations of state. For the CO_2 phase, the Span-Wagner equation of state is recommended (Span and Wagner, 1996), and for water the IF97 equation of state with salinity extensions are available in PFLOTRAN. Enthalpies of the solid gas hydrate (Handa, 1998) and salt (Lide and Kehiaian, 2020) phases are computed as functions of temperature. Several options for composite thermal conductivity can be used; the default thermal conductivity function is a linear scaling function of phase saturations:

$$\kappa = \kappa_{\text{dry}} + \phi \sum_{\alpha=l,g,h,i,s} s_\alpha \kappa_\alpha \tag{$\cancel{9}12$}$$

where κ_{dry} is the dry rock thermal conductivity and κ_α is the thermal conductivity of phase α.

The presence of salt has several impacts on system behaviour. ~~If present, s~~Solid salt precipitation can occur due to near-wellbore dry-out (water evaporating into the free CO_2 phase) during the injection period or due to rapid hydrate formation,

whereby water and CO_2 forming a hydrate excludes salt and thus increases dissolved salt concentrations. Salt precipitation reduces permeability, which affects CO_2 injectivity, gas flow, and liquid imbibition ~~during injection and very far into the future~~. This occurs either at the injection site if enough CO_2 is injected to dry out the water or far into the future when free phase CO_2 has undergone conversion to very high hydrate saturations (though at this point, permeability reduction due to salt precipitation is dwarfed by the presence of solid hydrate at high saturations). Aqueous dissolved salt concentration affects the density of the aqueous phase; the presence of gradients in salt concentration drives convective mixing. Salt exclusion during hydrate formation locally increases salt concentrations, which can produce this phenomenon (Fukuyama et al., 2023). Dissolved salt also affects gas solubility and shifts the three-phase equilibrium pressure of gas hydrate.

~~Carbon dioxide~~CO_2 equilibrium phase partitioning is computed using the method of Spycher and Pruess (2010); the CO_2 hydrate – free phase CO_2 – water three-phase equilibrium curve is determined from a polynomial fit of data from Men et al. (2022) up to ~~the upper quadruple point (~~283.2 K~~), beyond which point a steep line was used to preserve differentiability of the phase boundary~~ and then a linear function at higher temperatures (Figure 1). This 3-phase equilibrium boundary is consistent with the CO_2 hydrate phase boundary used in STOMP-HYD up to 100 MPa (McGrail et al., 2007) and is similar to the phase boundary proposed by Garapati et al. (2011) with the exception that here the phase boundary is monotonically increasing.~~.~~
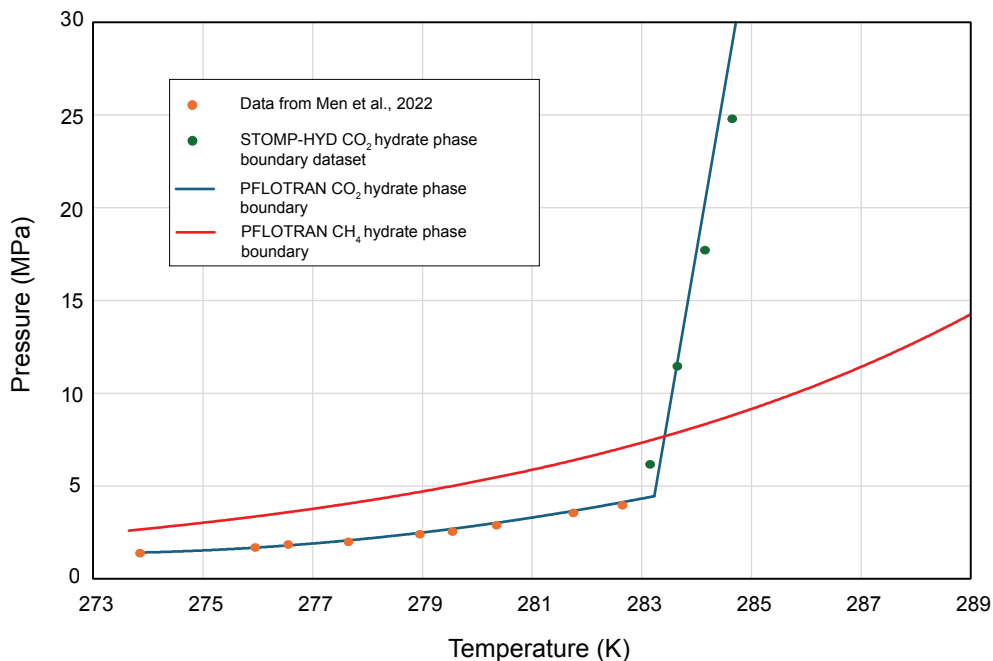
Figure 1: CO_2 hydrate phase boundary implemented in PFLOTRAN. At temperatures below 283.2 K, a curve fit of experimental data is used. Above 283.2 K, a line is used that is consistent with STOMP-HYD. The CH_4 hydrate phase boundary is plotted for reference (Moridis, 2003)

2.~~4~~3 Phase States and Primary Variables

PFLOTRAN's HYDRATE mode solves mass conservation, energy conservation, and well flux conservation equations for a set of three components (CH_4/CO_2/air, H_2O, NaCl) over five phases (aqueous, gas component-rich/gas, gas hydrate, ice, salt precipitate). This results in solving a set of four partial differential equations for all cells in the domain plus one coupled well equation per cell containing the bottom segment of a well. Therefore, PFLOTRAN's fully implicit solution solves for four primary variables everywhere plus one extra primary variable per well in the domain.

The reservoir (non-well) equations use primary variable switching depending on the thermodynamic state of a grid cell. HYDRATE mode contains 13 phase states with four primary variables per phase state (Table 1). For example, cells in the fully liquid (aqueous) saturated state solve for liquid pressure, dissolved gas mass fraction, temperature, and total salt mass per unit liquid mass as primary variables. Secondary variables like phase densities, viscosities, and enthalpies are computed at equilibrium from the primary variables through use of various equations of state. Precipitated salt saturation is computed by determining whether bulk salt concentration (total salt mass per mass of liquid phase) exceeds dissolved salt solubility and converting the excess salt mass into a solid phase (permeability updates according to Verma & Pruess, ~~[~~1988~~]~~). If dissolved gas mass fraction exceeds solubility and aqueous pressure, temperature, and dissolved salt mass fraction lie within the GHSZ ~~(i.e., at pressures and temperatures above the 3-phase equilibrium boundary)~~, the cell will transition into the hydrate-aqueous state and primary variables will update accordingly. Upon entering the hydrate-aqueous state, PFLOTRAN then switches primary variables and solves for gas pressure, hydrate saturation, temperature, and salt concentration.

Table 1: Phase states and primary variable combinations in PFLOTRAN's HYDRATE mode

Phase State	Primary Variables	Phase State	Primary Variables
L (aqueous)	P_l, x_l^g, T, m_l^s	AI (aqueous-ice)	P_l, x_l^g, S_l, m_l^s
G (gas component-rich)	P_g, P_a, T, m_b^s	HGA (hydrate-gas-aqueous)	S_l, S_h, T, m_l^s
GA (two-phase gas-aqueous)	P_g, S_g, T, m_l^s	HAI (hydrate-aqueous-ice)	P_g, S_l, S_i, m_l^s
HG (hydrate-gas)	P_g, P_a, T, m_b^s	HGI (hydrate-gas-ice)	S_i, S_h, T, m_b^s
HA (hydrate-aqueous)	P_g, S_h, T, m_l^s	GAI (gas-aqueous-ice)	P_g, S_g, T, m_l^s
HI (hydrate-ice)	P_g, S_h, T, m_b^s	HGAI (hydrate-gas-aqueous-ice)	S_l, S_g, S_i, m_l^s

GI (gas-ice)	P_g, S_i, T, $m_b{}^s$		

P_l = liquid pressure, P_g = gas pressure, P_a = gas-rich gas (air) component partial pressure, $x_l{}^g$ = aqueous dissolved gas mass fraction, T =
295   temperature, $m_l{}^s$ = salt mass fraction per unit aqueous mass, $m_b{}^s$ = total salt mass per unit bulk volume, S_g = gas saturation, S_h = hydrate
saturation, S_l = liquid saturation, S_i = ice saturation

For the well equation, the bottom-hole pressure (BHP) of the well is solved as a primary variable. Given a user-defined well flow rate, each well's bottomhole pressureBHP is solved fully implicitly as part of the full reservoir flow solution. At a given

300   bottomhole pressureBHP, the well model solves for all other pressures in the well by working upward and iteratively solving hydrostatic pressure of the injection fluid where variable fluid density in the well is updated as a function of pressure and temperature. Once the hydrostatic pressures are determined, mass and energy fluxes between well and reservoir at the well segment centroids are computed by adding a hydrostatic adjustment to reservoir pressures to align reservoir pressures with well segment centroids and then employing Equation 74. Fluxes between coupled wells and reservoir cells are therefore

305   functions of the well primary variable (bottomhole pressureBHP) and reservoir cell primary variables (e.g., gas/liquid pressure).

Using fully implicit coupling and a Newton-Raphson solution search method, insertion of a coupled well into the domain therefore adds additional fill to the Jacobian matrix used to compute solution updates. Critically, the well model adds extra

310   connectivity beyond the typical stencil for two-point flux calculations. Thus, the structure of the Jacobian matrix is altered by introducing wells. This alteration is typically minimal, but it would likely become more severe computationally demanding as the number of wells in the domain is increased or as the number of uncased (i.e., screened) segments per well is increased. The number of wells, the extent to which each well increases the fill of the Jacobian, and the strength of the coupling between well and reservoir are all likely to affect the overall performance of simulations using the coupled well model. PFLOTRAN uses

315   neighbour cell ghosting to parallelize computations: for a given subset of grid cells in the model domain that are owned by a particular process, say, Process "N", all of the off-process grid cells that border these cells are "ghosted" onto Process "N", meaning copies of state variables for those cells are kept up to date for computing updated flux terms at processor boundaries. Cell ghosting is determined by the numerical stencil and the distribution of cells on processors in parallel. Since adding a well introduces connectivity beyond the original ; the fully coupled well model updates thestencil, PFLOTRAN updates the

320   ghosting stencil to include all off-process reservoir cells connected by a given well, allowing for consistent full incorporation of well terms in the Jacobian both in parallel and in serial. When a well is turned off (or well flow rates are set to 0), that well equation is not solved.

3 Results

We demonstrate our developments by applying the software to a set of two hypothetical CO_2 injection scenarios in marine environments within the GHSZ. In the first example, liquid CO_2 is injected slowly into a simple 1D homogeneous sediment column through a partially screened well beneath the GHSZ. The second example simulates commercial-scale injection of supercritical CO_2 into a 2D radial domain with heterogeneous layering, where a well is screened within and beneath the GHSZ. The CO_2 plume in this model is tracked for 10,000 years as it transitions from a supercritical phase to a dense liquid phase and then into the gas hydrate phase.

3.1 1D Liquid CO_2 Injection into a Homogeneous Reservoir

In this scenario, a relatively slow ~~trickle~~ injection is designed to illustrate the multiphase and thermodynamic processes associated with injecting CO_2 into the GHSZ. A 1D, ~~500~~1,000-m homogeneous domain is initialized to hydrostatic conditions where the top of the domain is held at seafloor pressure of 10 MPa, ~~seafloor temperature~~bottom water temperature of ~~3°~~5° C, and geothermal gradient of ~~30°~~20° C/km. The top Dirichlet boundary condition is set to the initial ~~seafloor temperature~~bottom water temperature, pressure, zero gas mass fraction, and constant salinity (0.035 kg/kg). The bottom boundary at ~~500~~1,000 mbsf is a Neumann zero flux boundary. The domain is discretized into ~~100~~200 grid cells in the vertical dimension; individual grid cells measure 25 m in the horizontal x-dimension by 1 m in the horizontal y-dimension by 5 m in the vertical z-dimension. A well ~~penetrates the entire domain and is~~extends to 500 meters below seafloor (mbsf) and is ~~uncased (i.e.,~~ screened~~)~~ for ~~20~~25 m from 475 ~~meters below seafloor (~~mbsf~~)~~ to ~~495~~500 mbsf. Dense liquid phase CO_2 is injected at 20° C at an injection rate of 15,000 kg/yr for ~~1~~50 years. Pressure of the injection varies along the well depending on the ~~BHP~~bottomhole pressure, but CO_2 remains in the liquid phase for the entirety of the injection. Use of the well model will lead to variable CO_2 injection rates in each of the ~~uncased~~ screened well segments and correspondingly variable injection enthalpy as a function of well segment pressure; this effect is less noticeable in this homogeneous case than in the heterogeneous case. This simulation is run for 200 years. While it is likely that bottom water temperature would fluctuate over 200 years, bottom water temperature variation is site specific; PFLOTRAN can apply time-dependent bottom water temperature as a boundary condition, but for this study a constant temperature was used for simplicity. A constant reservoir porosity is set to 0.35, and constant isotropic permeability is set to 1×10^{-13} m^2. A Van Genuchten capillary pressure function is used, where Van Genuchten ~~n~~m is set to ~~1.8416~~20.5, $\alpha =$ ~~0.5~~1x10^{-4} ~~m~~Pa^{-1}, and $S_{lr} =$ 0.05. Corey relative permeability functions are used, where $m =$ 0.~~45~~75, $S_{lr} =$ 0.3 and $S_{gr} =$ 0.05.
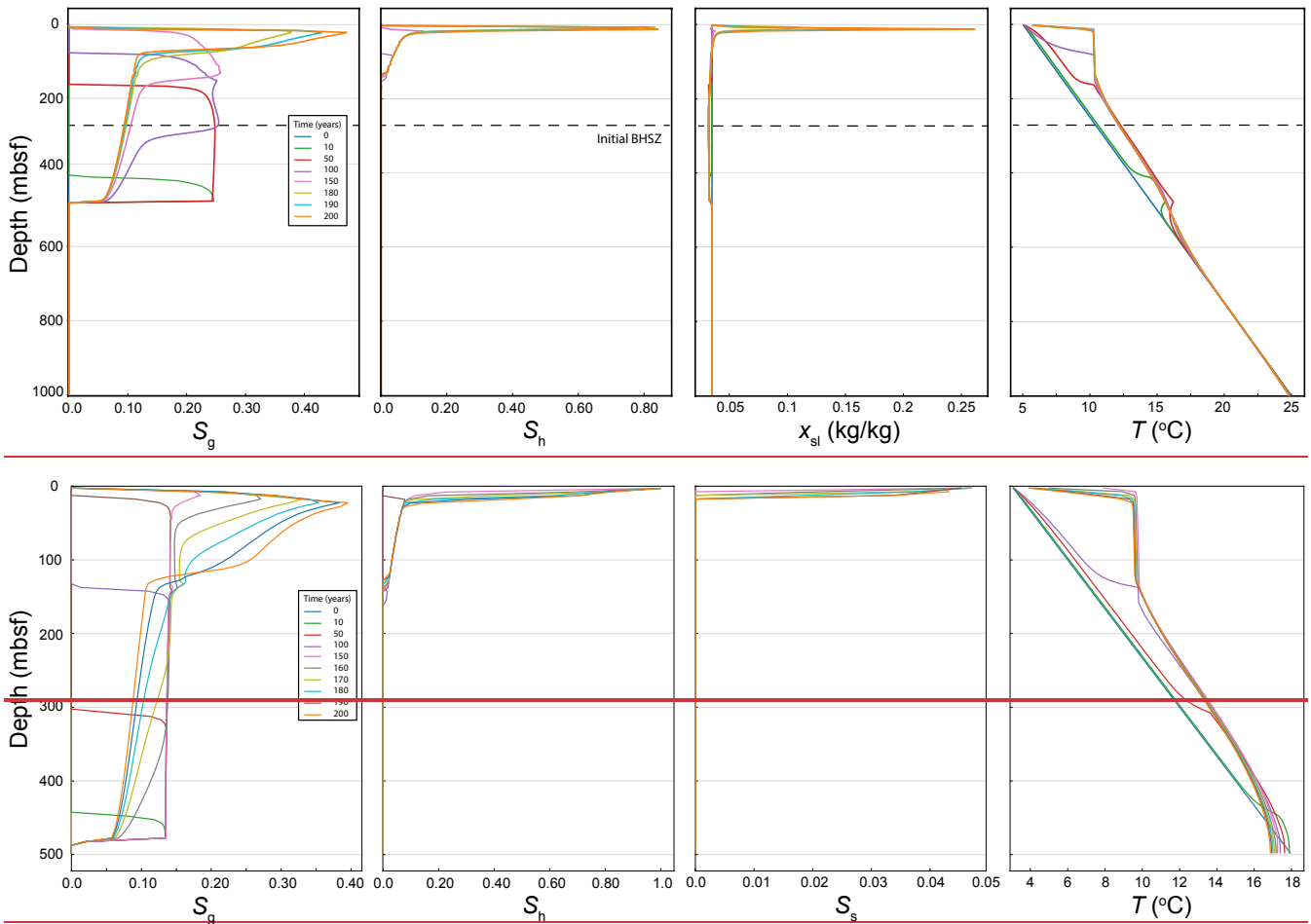
~~Figure 1~~Figure 2: Gas saturation, hydrate saturation, dissolved salt ~~precipitate saturation~~mass fraction, and temperature during and after a CO_2 injection beneath the GHSZ. Dashed line indicates the initial (pre-injection) BHSZ, though this is perturbed by upward migration of warm gas.

During the ~~first~~ 50 years of injection, the injected CO_2 remains beneath the base of the CO_2 hydrate stability zone (~~Figure 1~~Figure 2). Therefore, it can only exist as free-phase CO_2. CO_2~~Thus, it~~ migrates upward in characteristic fashion: buoyancy and pressure forces drive gas (free-phase CO_2) saturations exceeding the residual gas saturation to migrate upward in the sediment column. By 100 years, the free-phase CO_2 front has reached the base of the GHSZ. At this point, some free-phase CO_2 converts to CO_2 hydrate. Exothermic hydrate formation keeps the reservoir temperature at the three-phase equilibrium temperature while free-phase CO_2 and hydrate coexist. As the gas plume migrates upward over time, more gas converts into gas hydrate. While the gas supply is strong and hydrate is still forming, the temperature of the reservoir is pushed well above the background (initial) geothermal temperature. The CO_2 hydrate 3-phase equilibrium temperature is ~~cannot form past~~

365 approximately 10º C at this depth, which is why the temperature throughout the three-phase zone ~~is fixed to~~remains at roughly 10º C.

After the injection period ends, hydrate accumulates in high saturations near the top of the domain due to the ~~seafloor temperature~~bottom water temperature and pressure being fixed; the resulting permeability reduction causes gas to pool and
370 salt to concentrate where hydrate is forming, leading to salt precipitation. This kind of scenario is unlikely to occur in a more realistic reservoir in 2D and 3D where permeability reduction would cause gas to migrate laterally and therefore not cause such significant pooling effects. But this model illustrates how exothermic hydrate formation can lead to a thick (albeit transient) three-phase stability zone throughout which free-phase CO_2 can remain mobile. Therefore, the fact that CO_2 hydrate is stable in the upper hundred meters of sediments at a particular hydrostatic pressure and geothermal temperature is an
375 insufficient condition for ensuring CO_2 trapping by hydrate formation. ~~merely relying on conversion of CO₂ to gas hydrate alone as a CO₂ trapping mechanism is likely insufficient due to the thermal buffering effect of exothermic hydrate formation.~~ Permeability reduction associated with gas hydrate formation can act to slow free-phase CO_2 migration, but, at least at early time, a combination of thermodynamic and other structural trapping mechanisms is likely necessary to ensure the long-term sequestration of most of the injected CO_2 in the subsurface GHSZ.

380 **3.2 Supercritical CO₂ Injection into a 2D Heterogeneous Reservoir**

In this scenario, a commercial-scale CO_2 injection is modelled under more realistic reservoir and injection conditions (~~Figure 2~~Figure 3). A 2D, heterogeneous cylindrical domain extends from the seafloor down to 600 mbsf with a radius of 3.765 km. The model domain consists of 40 grid cells in the horizontal dimension increasing in thickness from 7.38 m at the model centre to 364.36 m at the far edge. The model contains 55 cells in the vertical dimension with varying thickness, each corresponding
385 to a different layer in the model. The model consists of interbedded sand and mud units as might be found within the marine GHSZ. High and low permeability layers alternate with synthetic heterogeneity; similarly, the model contains heterogeneous porosity and capillary entry pressure. All other physical properties are kept constant between layers. A Brooks-Corey capillary pressure function along with Burdine relative permeability functions for liquid and gas phases are used for all layers. For all layers, Brooks-Corey λ =0.8311 and $S_{rl} = S_{rg} = 0.0597$. The capillary entry pressure (the inverse of which is expressed by the
390 Brooks-Corey α parameter) varies between reservoir layers (~~Figure 3~~Figure 4). Rock density is set to 2,650 kg/m³, dry rock thermal conductivity is set at 2.0 W/m-C, and soil compressibility is modelled with a linear compressibility function using a soil compressibility of 1.0E-8 Pa^{-1} and a reference pressure of 10 MPa. Seafloor pressure is set to 10 MPa, ~~seafloor temperature~~bottom water temperature is 5º C, and seafloor salinity is 0.035 kg/kg. The model is initialized at hydrostatic pressure, constant salinity, and a geothermal gradient of 20º C/km. The top and outer edges of the domain are kept at the initial
395 conditions. The bottom boundary condition is set to no liquid or gas flux, constant salinity, and a constant heat flux to preserve the geothermal gradient.

The well used in this scenario extends from the seafloor to 300 mbsf and is cased for the first 100 m. The rest of the well is ~~uncased~~screened; flow from well to reservoir is possible only in the ~~uncased~~ screened interval. Given the conditions outlined

400 above, the ~~bulk BHSZ~~ initial BHSZ for CO_2 hydrate is at approximately 250 mbsf. Therefore, the well in this scenario extends through the GHSZ and 50 m below the ~~bulk BHSZ~~initial BHSZ. Care was taken to ensure that the required well pressures to achieve the specified CO_2 injection rate were realistic; the 100 m depth of well casing was chosen so that the well pressures resulting from our prescribed injection rate did not exceed the lithostatic pressure. This calculation is approximate and does not consider the fracture gradient; the fact that well pressures can easily approach the lithostatic gradient in these settings

405 means that reservoir integrity should be rigorously evaluated when performing site-specific evaluations of CO_2 injectivity in the shallow subsurface.

CO2 Injection rate: 1 MMt/yr, 45° C

$P_{seafloor}$ = 10 MPa
$T_{seafloor}$ = 5° C
Salinity$_{seafloor}$ = 0.035 kg/kg

3765 m

g

600 m

Well

Geothermal Gradient = 20° C/km

No Liquid or Gas Flux
Heat Flux = 0.05 W/m^2
Salinity = 0.035 kg/kg
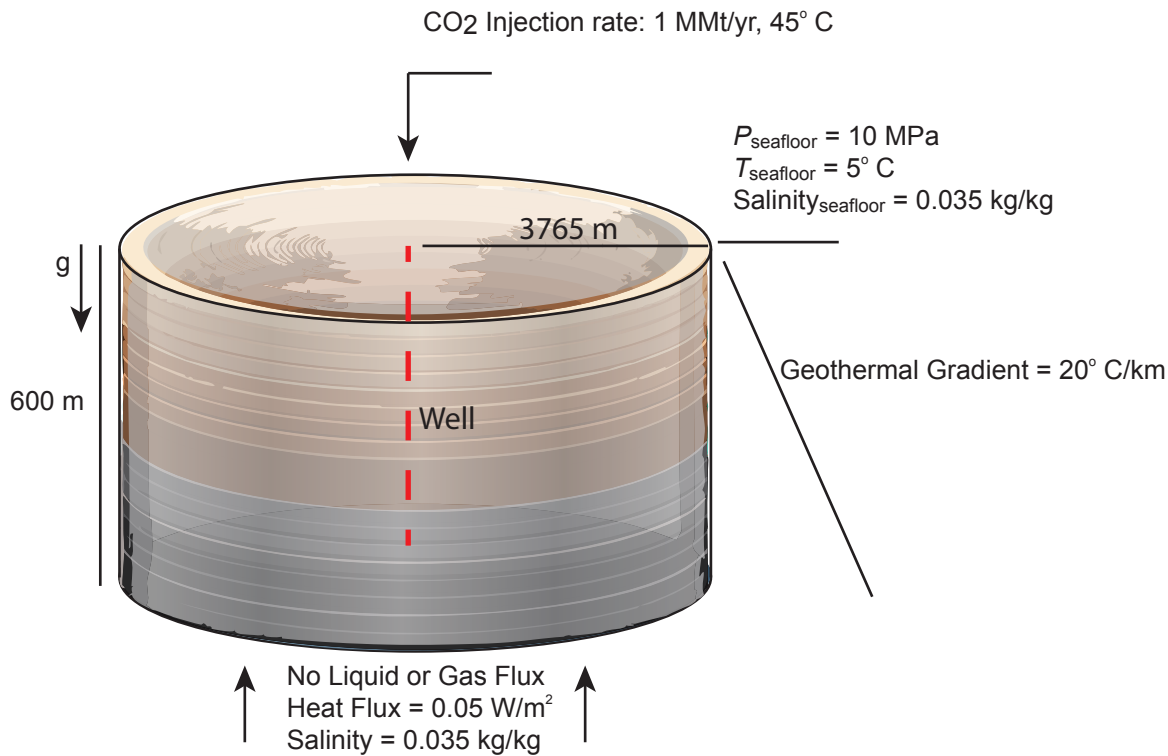
~~Figure 2~~Figure 3: ~~Schematic of the h~~Illustration of a heterogeneous layered 2D cylindrical mode~~l, with specific model parameters labeled~~l injection scenario

410

The model is run for 10,000 years. ~~The injection is designed as if the reservoir were a prospective DOE CarbonSAFE storage complex. Therefore,~~: CO_2 is injected continuously at a rate of 1 million metric tons (MMT) per year for 50 years to meet a storage target of 50 MMT of CO_2. The CO_2 is injected at a constant temperature of 45° C; injection pressure will vary along the wellbore depending on the hydrostatic pressure of the well, and this in turn will affect the enthalpy of the injected gas.

415   After 50 years, the well is shut off; over time, warm supercritical CO_2 will cool into a dense liquid CO_2 phase and then eventually a gas hydrate phase.
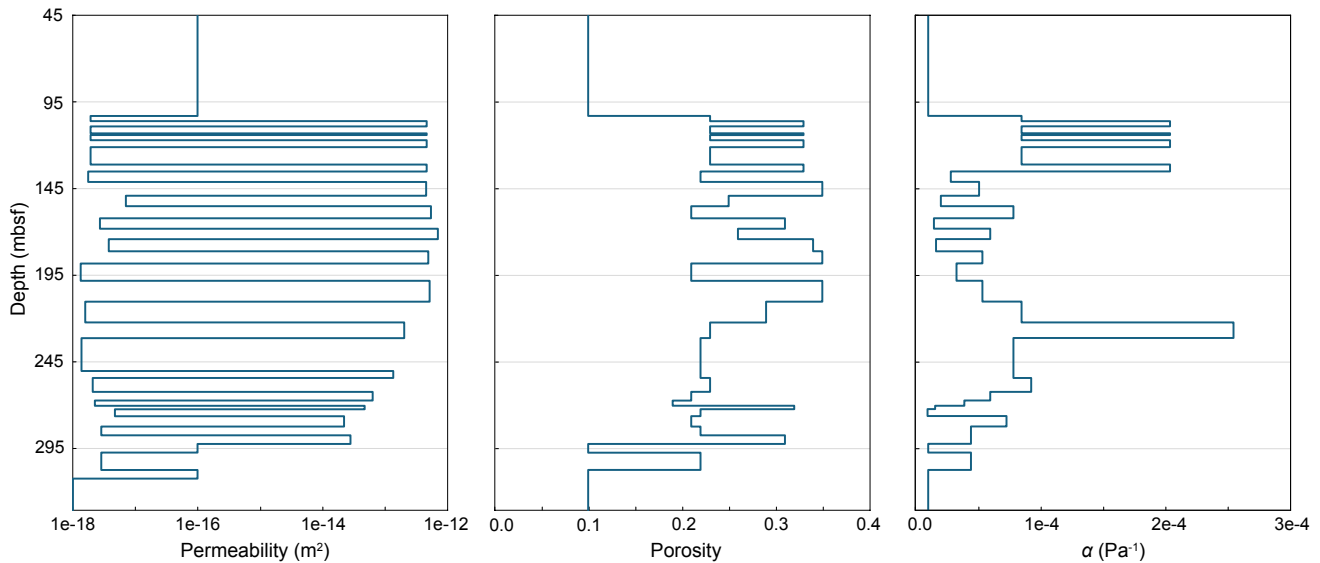
~~Figure 3~~Figure 4: Depth-varying physical properties _(permeability, porosity, and inverse capillary entry pressure [α])_ of the
420   **heterogeneous 2D injection scenario~~, zoomed in~~ near the injection interval. Physical properties held constant above and below these snapshots.**

During the 50-year injection interval, gas flows predominantly into the high-permeability reservoir intervals (Figure ~~4~~5, Figure
~~5~~6). This is because the well model adjusts _how the mass of injected CO_2 is distributed to each interval in the injection region_
425   _(Figure 7) given_ the _total_ gas ~~flow~~injection rate_,_ ~~(Figure 6) into individual intervals as a function of~~hydrostatic well pressure, reservoir pressure, and well index, where well index is a function of reservoir permeability. Since early hydrate formation in the reservoir units elicits a permeability and pressure response, the well flow rate into individual units evolves over time during the injection. In some units, well flow rate drops, and these drops are then compensated by increases in flow rates in other units. Likewise, the pressure in the well evolves over time in response to hydrate formation and relative permeability of the
430   mobile fluids.

By the end of the injection period, gas has flowed preferentially in the radial direction along high permeability flow paths. On the outer edges of the gas plume, free phase CO_2 combines with water to form a gas hydrate phase where pressures and temperatures are within the gas hydrate stability zone. Since pure CO_2 is being injected through the well and since water is
435   miscible in the CO_2 phase, high gas saturations in the near-wellbore cells cause salt concentrations in those cells to increase

above salt solubility. This salting out effect results in small amounts of salt precipitate saturation in the pore space at the end of the injection.
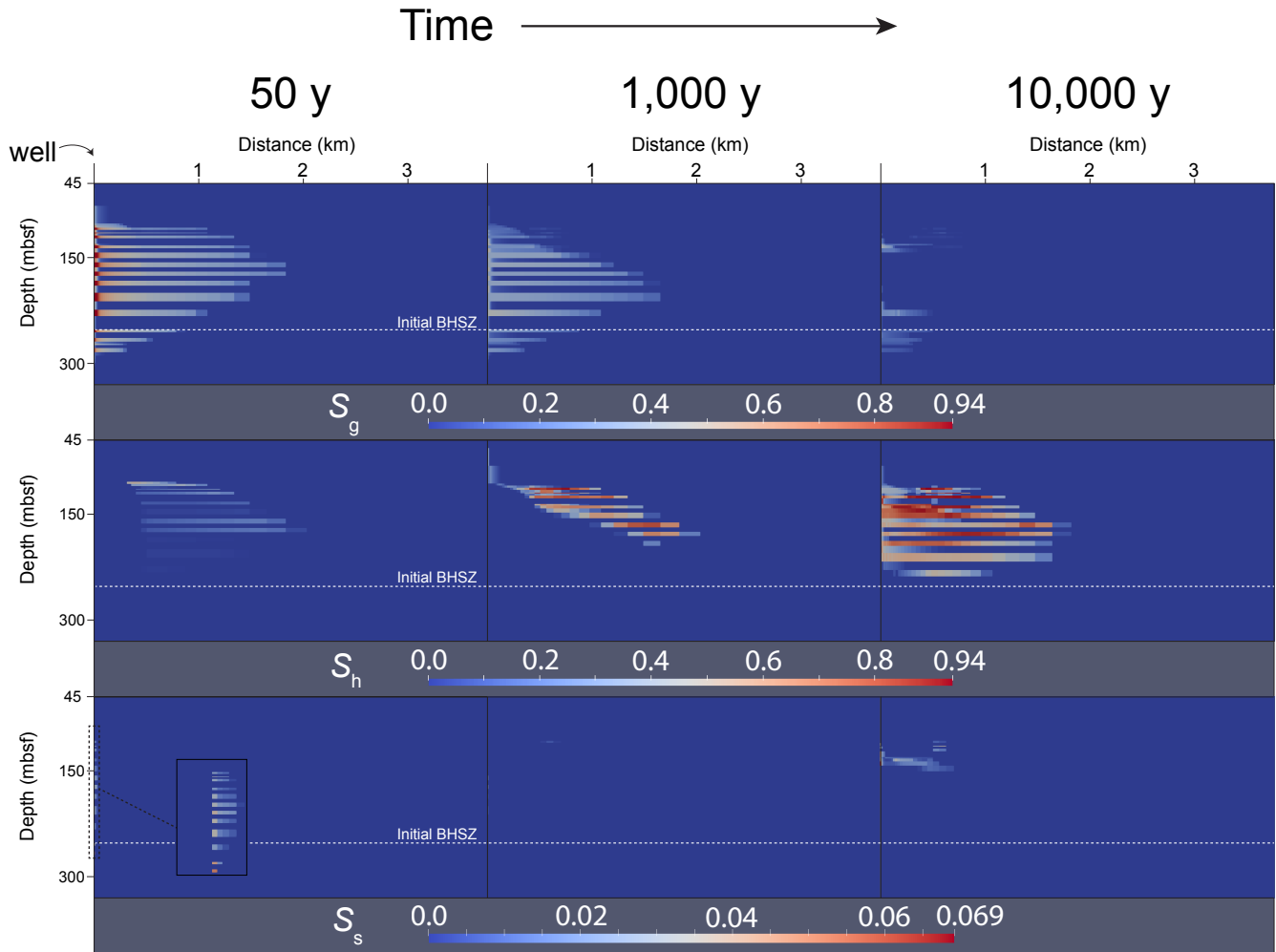
Figure 4̶5: Snapshots of saturations over time in the vicinity of the wellbore. Depth is represented by the vertical axis, and radial distance from the well is represented by the horizontal axis. Gas (free-phase CO₂) saturation (S_g), hydrate saturation (S_h), and salt precipitate saturation (S_s) distribution at 50 years, 1,000 years, and 10,000 years of simulation time. A zoomed-in cut-out shows near-wellbore salt precipitate saturations at 50 years.

As water imbibes back into the near-wellbore cells between 50 and 1,000 years, gas saturations in those cells drop and salt re-dissolves (salt precipitate saturations near the wellbore drop toward 0). During this time, the temperature of the injected fluid is dropping toward the ~~background temperature field~~initial geothermal temperature. As this happens, free phase CO₂ combines with available water to form gas hydrate. Exothermic hydrate formation props up temperatures during hydrate formation and

slows the process of CO₂ conversion into gas hydrate. In some areas at the upper edges of the CO₂ plume, where the system is furthest into the GHSZ, very high conversion of CO₂ to gas hydrate is achieved in a relatively short amount of time. Since hydrate formation only involves water and CO₂ components, salt exclusion during rapid hydrate formation results in local buildup of salt concentrations. Some cells in the model associated with rapid hydrate formation therefore exhibit some solid salt precipitation by 1,000 years.
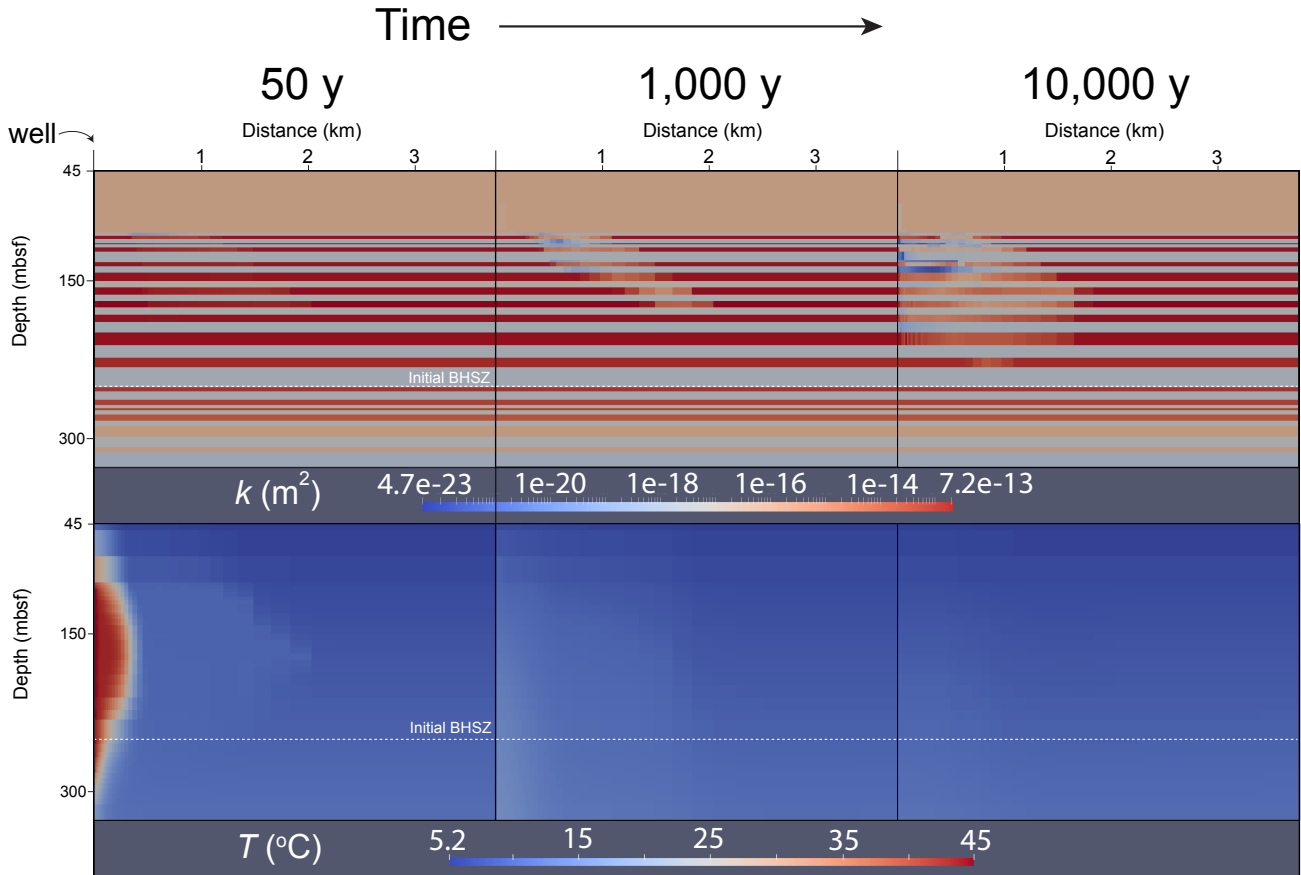
Figure 5̶6̲: Permeability (k) and temperature (T) distribution at 50 years, 1,000 years, and 10,000 years of simulation time. Depth is represented by the vertical axis, and radial distance from the well is represented by the horizontal axis.

After 10,000 years, most of the injected CO₂ has converted into gas hydrate. High gas hydrate saturations have built up in the near-wellbore area since the initial temperature of the injection has decayed away toward the steady-state geothermal temperature profile. Hydrate formation has significantly decreased the permeability of the host reservoir, and gas has migrated into the other layers to form hydrate. A region of three-phase coexistence (liquid water, free phase CO₂, and gas hydrate) is still present after 10,000 years because of a combination of exothermic hydrate formation and slow imbibition rates of cool liquid water due to significant permeability reduction.

465
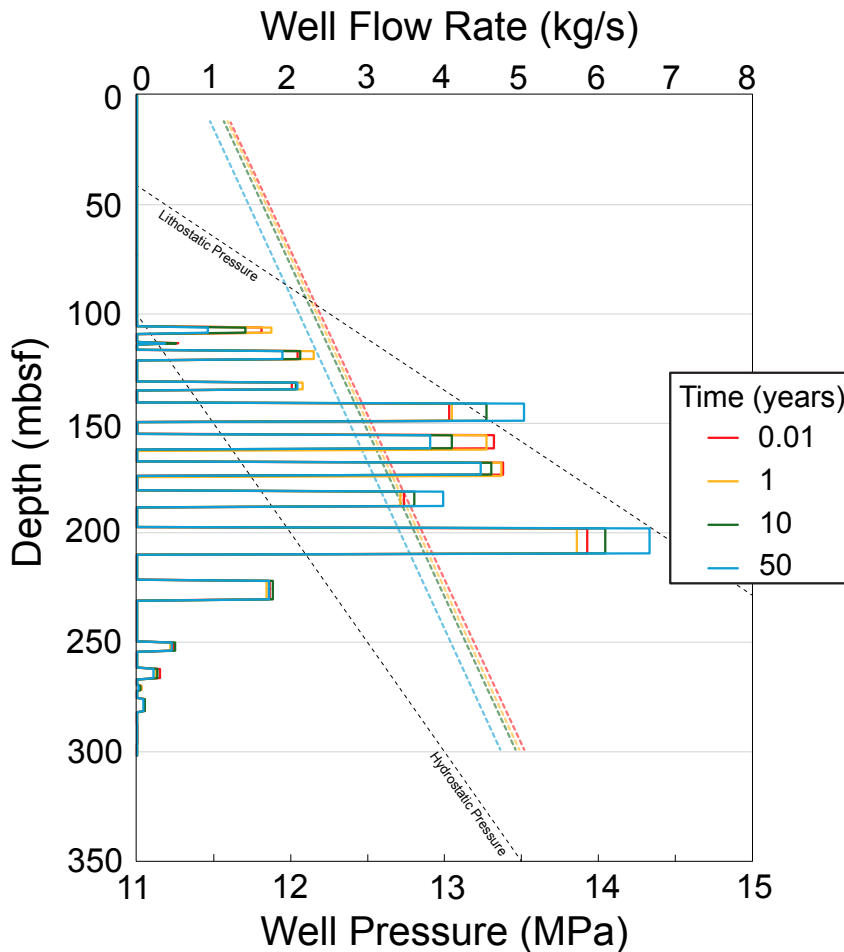
Figure ~~6~~7: CO₂ mass flow rate in each well segment (solid lines) and supercritical CO₂ phase pressure in the well (dashed lines) during the 50-year injection period.

Discussion

470   The two models presented here were selected to demonstrate some of the key dynamic coupled processes associated with CO₂ injection into the gas hydrate stability zone. In the 1D homogeneous model, CO₂ is injected beneath the GHSZ and forms a free phase which migrates upward due to buoyancy and pressure forces. Once it enters the GHSZ, conversion of CO₂ into an immobile hydrate phase is limited by the rate at which heat can diffuse away and availability of water. When thermal conduction and liquid water flow are limited, the system can maintain 3-phase equilibrium temperature for decades (or

475   thousands of years as is shown in the 2D model). This thermal buffering phenomenon has been observed in models of natural

methaneCH$_4$ hydrate formation and dissociation in marine sediments and can occur on geologic timescales depending on free gas phase flow rate or rate of environmental change (You and Flemings, 2018; Oluwunmi et al., 2022). Clearly, such a scenario would not be ideal for permanent CO$_2$ sequestration as much of the CO$_2$ remains in a free phase and accumulates very close to the seafloor. Permeability reduction due to hydrate formation adds a physical trapping mechanism analogous to a low permeability sealing facies. The fact that this permeability reduction is the primary mechanism for preventing CO$_2$ flow to the surface in the 1D model suggests that physical/structural trapping should be considered just as important or more important than thermodynamic trapping when evaluating a reservoir within the GHSZ for long-term CO$_2$ storage.

The 2D cylindrical model was designed to incorporate more realistic reservoir physical properties and include an injection rate more viable for commercial-scale CO$_2$ storage in the GHSZ. In this scenario, CO$_2$ was injected into a layered reservoir that is bounded by low permeability facies that inhibit direct flow of CO$_2$ to the seafloor. Instead of injecting beneath the GHSZ, a high-temperature supercritical CO$_2$ phase is injected directly into and directly beneath the GHSZ. Near-wellbore gas hydrate formation is prevented by the high temperature of the injection during the injection period. Hydrate formation does occur during the injection period at the edges of the CO$_2$ plume; the associated changes in fluid mobility and permeability alter the pressure in the well and cause well flow rates to fluctuate layer-by-layer. Therefore, even if the CO$_2$ injection temperature is designed to prevent near-wellbore hydrate formation, hydrate formation in the far-field should be considered when designing a CO$_2$ injection insofar as it could appreciably affect wellbore pressure. Salt precipitation can occur near the wellbore during injection due to "salting out" effects of dry CO$_2$ injection. Salt can also precipitate later in time as CO$_2$ converts to hydrate faster than the pore water can freshen through either aqueous imbibition or salt diffusion. In either case, salt precipitate saturations appear to be minimal for the scenario modelled here, but salt precipitation could appreciably decrease permeability under a configuration with either more rapid CO$_2$ injection or more rapid conversion of CO$_2$ to hydrate. In some regions of this model, hydrate saturations become very high at late times and lower the permeability of host reservoir units by several orders of magnitude. This makes for effective sealing of CO$_2$ by conversion to an immobile phase and by impeding flow of the free CO$_2$ phase. This phenomenon also has the effect of pushing gas into less intrinsically permeable layers and ultimately smoothing the distribution of gas hydrate throughout the model domain.

Potential leakage of CO$_2$ into the ocean at the seafloor is clearly a risk when injecting CO$_2$ into shallow marine reservoirs. In this model, advective leakage of CO$_2$ is prevented by the low permeability of the top facies, but CO$_2$ still migrates upward diffusively and thus there is some diffusive leakage of CO$_2$ at the seafloor. Beyond just considering the bulk permeability of the top facies, however, care should also be taken to inject CO$_2$ at pressures that remain below the fracture pressure of the overburden. While we do not model permeability evolution due to fracturing in this model, we designed our model scenarios to avoid fracturing (well model pressures in the injection interval were designed to remain below the lithostatic pressure). In a site-specific scenario, the fracture gradient should be well characterized and incorporated into CO$_2$ injection design.

510 Although the models presented here only consider injection of CO_2 into reservoirs without naturally occurring gas hydrate deposits, the presence of other hydrates (e.g., CH_4 hydrate) in a reservoir could affect the injectivity of CO_2 by altering the physical properties (e.g., permeability) of the reservoir. The stability of all potential hydrates could be altered by injection of CO_2, so site characterization should consider whether and what kinds of hydrates might exist in a potential subsea host reservoir. This information could be used to parameterize heterogeneous initial physical properties of a model, modify phase
515 behaviour as a function of gas mixtures, or to develop a more sophisticated model of the interactions between multiple gases forming/dissolving multiple hydrates, but such models are beyond the scope of this work.

Conclusions

We present several new developments in PFLOTRAN's HYDRATE mode including a new option to model CO_2 as the working gas, a new salt mass balance for considering effects of salinity gradients and salt precipitation, and a new fully coupled
520 hydrostatic well model. We demonstrate these new capabilities on ~~a series of~~two test problems designed to explore the coupled processes relevant to CO_2 injection into the marine gas hydrate stability zone for the purpose of permanently sequestering CO_2. CO_2 sequestration in the gas hydrate stability zone is a potentially promising technique for secure storage of CO_2 because of the associated favourable conditions for converting injected CO_2 into solid gas hydrate form, which is immobile in the pore space. However, no reservoir modelling studies to date have demonstrated what commercial-scale CO_2 injection into the gas
525 hydrate stability zone might look like. We show through a 1D homogeneous model that it is critical to consider multiple trapping mechanisms in addition to the thermodynamic trapping accompanied by conversion of CO_2 into hydrate form. We then expand to a 2D heterogeneous cylindrical model with a commercial-scale 1 MMT/yr CO_2 injection rate to underscore the interplay between structural trapping, thermodynamics, and permeability alteration on the migration and conversion of CO_2. We demonstrate how our fully implicit well model adapts to changes in flow properties during CO_2 injection, and how injection
530 of a warm supercritical CO_2 phase can facilitate near-wellbore injectivity but can lead to pressure change in the well. In the future, this capability could be used to more rigorously evaluate the potential for secure CO_2 storage in greater volumes, at larger (3D) scales, with more site-specific inputs, and with more exotic well designs including multiple wells or horizontal wells.

Code and Data Availability

535 The software developments described here were released on August 23, 2024 with PFLOTRAN version 6.0 (www.pflotran.org). PFLOTRAN is open source and freely available under a GNU LGPL Version 3 license at https://bitbucket.org/pflotran/pflotran. Software inputs and a snapshot of the PFLOTRAN v6.0 Bitbucket repository are available on Zenodo at https://zenodo.org/records/13619874. The files on Zenodo include PFLOTRAN input decks for both model scenarios and associated Span-Wagner EOS database files referenced by those input decks.

540 **Acknowledgements**

This research was supported by the U.S. Department of Energy (DOE) Office of Fossil Energy and Carbon Management and the National Energy Technology Laboratory (NETL), Award No. FWP 72688. This work was also supported by Pacific Northwest National Laboratory's (PNNL) Laboratory-Directed Research and Development (LDRD) program, Award No. 211622. PNNL is operated for the DOE by Battelle Memorial Institute under contract DE-AC05-76RL01830. This paper

545 describes objective technical results and analysis. Any subjective views or opinions that might be expressed in the paper do not necessarily represent the views of the U.S. Department of Energy or the United States Government. Generative AI was used to develop part of the schematic illustration in ~~Figure 2~~Figure 3.

Author Contribution:

550 MN: software development, model conceptualization, formal analysis, methodology, writing; JB: model conceptualization, writing; FN: model conceptualization, writing; GH: software development, review & editing.

Competing Interests: The authors declare that they have no conflict of interest.

References

555 Al Hameli, F., Belhaj, H., & Al Dhuhoori, M. (2022). CO2 sequestration overview in geological formations: Trapping mechanisms matrix assessment. *Energies*, *15*(20), 7805.

Anderson, R., Llamedo, M., Tohidi, B., & Burgass, R. W. (2003). Experimental measurement of methane and carbon dioxide clathrate hydrate equilibria in mesoporous silica. *The Journal of Physical Chemistry B*, *107*(15), 3507-3514.

560

Belgodere, C., Dubessy, J., Vautrin, D., Caumon, M. C., Sterpenich, J., Pironon, J., ... & Birat, J. P. (2015). Experimental determination of CO2 diffusion coefficient in aqueous solutions under pressure at room temperature via Raman spectroscopy: impact of salinity (NaCl). *Journal of Raman Spectroscopy*, *46*(10), 1025-1032.

565 Cadogan, S. P., Maitland, G. C., & Trusler, J. M. (2014). Diffusion coefficients of CO2 and N2 in water at temperatures between 298.15 K and 423.15 K at pressures up to 45 MPa. *Journal of Chemical & Engineering Data*, *59*(2), 519-525.

Clennell, M. B., Hovland, M., Booth, J. S., Henry, P., & Winters, W. J. (1999). Formation of natural gas hydrates in marine sediments: 1. Conceptual model of gas hydrate growth conditioned by host sediment properties. *Journal of Geophysical*

570 *Research: Solid Earth*, *104*(B10), 22985-23003.

Collett, T. S. (2000). Natural gas hydrate as a potential energy resource. In *Natural Gas Hydrate: In Oceanic and Permafrost Environments* (pp. 123-136). Dordrecht: Springer Netherlands.

Dai, S., & Seol, Y. (2014). Water permeability in hydrate-bearing sediments: A pore-scale study. *Geophysical Research Letters*, *41*(12), 4176-4184.

Eymold, W. K., Frederick, J. M., Nole, M., Phrampus, B. J., & Wood, W. T. (2021). Prediction of gas hydrate formation at Blake Ridge using machine learning and probabilistic reservoir simulation. *Geochemistry, Geophysics, Geosystems*, *22*(4), e2020GC009574.

Frederick, J. M., Eymold, W. K., Nole, M. A., Phrampus, B. J., Lee, T. R., Wood, W. T., ... & Conley, E. (2021). *Forecasting marine sediment properties with geospatial machine learning* (No. SAND2021-10675). Sandia National Lab. (SNL-NM), Albuquerque, NM (United States).

Fu, X., Waite, W. F., & Ruppel, C. D. (2021). Hydrate formation on marine seep bubbles and the implications for water column methane dissolution. *Journal of Geophysical Research: Oceans*, *126*(9), e2021JC017363.

Fukuyama, D., Daigle, H. C., Nole, M. A., & Song, W. (2023). Onset of convection from hydrate formation and salt exclusion in marine sands. *Earth and Planetary Science Letters*, *605*, 118039.

Garapati, N., Velaga, S., & Anderson, B. J. (2011, July). Development of a thermodynamic framework for the simulation of mixed gas hydrates: Formation, dissociation, and CO2-CH4 exchange. In *Proceedings of the 7th International Conference on Gas Hydrates (ICGH 2011), Edinburgh, Scotland, United Kingdom.*

Gauteplass, J., Almenningen, S., Ersland, G., Barth, T., Yang, J., & Chapoy, A. (2020). Multiscale investigation of CO2 hydrate self-sealing potential for carbon geo-sequestration. *Chemical Engineering Journal*, *381*, 122646.

Goldberg, D., Aston, L., Bonneville, A., Demirkanli, I., Evans, C., Fisher, A., ... & White, S. (2018). Geological storage of CO2 in sub-seafloor basalt: the CarbonSAFE pre-feasibility study offshore Washington State and British Columbia. *Energy Procedia*, *146*, 158-165.

Haas, J. L. (1976). Physical properties of the coexisting phases and thermochemical properties of the H2O component in boiling NaCl solution. *Geol. Surv. Bull., A*, *1421*, 73.

Hammond, G. E., Lichtner, P. C., & Mills, R. T. (2014). Evaluating the performance of parallel subsurface simulators: An illustrative example with PFLOTRAN. *Water resources research*, *50*(1), 208-228.

Handa, Y. P. (1988). A calorimetric study of naturally occurring gas hydrates. *Industrial & engineering chemistry research*, *27*(5), 872-874.

Kaminski, P., Urlaub, M., Grabe, J., & Berndt, C. (2020). Geomechanical behaviour of gassy soils and implications for submarine slope stability: a literature analysis. *Geological Society, London, Special Publications*, *500*(1), 277-288.

Koh, D. Y., Kang, H., Lee, J. W., Park, Y., Kim, S. J., Lee, J., ... & Lee, H. (2016). Energy-efficient natural gas hydrate production using gas exchange. *Applied Energy*, *162*, 114-130.

Lane, J., Greig, C., & Garnett, A. (2021). Uncertain storage prospects create a conundrum for carbon capture and storage ambitions. *Nature Climate Change*, *11*(11), 925-936.

Leverett, M. C. (1941), Capillary behavior in porous solids, Trans. Am. Inst. Min. Metall. Pet. Eng., 142(1), 152–169, doi:10.2118/941152-G.

Liu, X., & Flemings, P. B. (2011). Capillary effects on hydrate stability in marine sediments. *Journal of Geophysical Research: Solid Earth*, *116*(B7).

Lide, D. R., & Kehiaian, H. V. (2020). *CRC handbook of thermophysical and thermochemical data*. CRC press.

McGrail, B. P., Schaef, H. T., White, M. D., Zhu, T., Kulkarni, A. S., Hunter, R. B., ... & Martin, P. F. (2007). *Using carbon dioxide to enhance recovery of methane from gas hydrate reservoirs: final summary report* (No. PNNL-17035). Pacific Northwest National Lab.(PNNL), Richland, WA (United States).

Men, W., Peng, Q., & Gui, X. (2022). Hydrate phase equilibrium determination and thermodynamic modeling of CO2+ epoxy heterocycle+ water systems. *Fluid Phase Equilibria*, *556*, 113395.

Moridis, G. J. (2003). Numerical studies of gas production from methane hydrates. *Spe Journal*, *8*(04), 359-370.

Nole, M., Daigle, H., Cook, A. E., Malinverno, A., & Flemings, P. B. (2018). Burial-driven methane recycling in marine gas hydrate systems. *Earth and Planetary Science Letters*, *499*, 197-204.

Oluwunmi, P., Pecher, I., Archer, R., Reagan, M., & Moridis, G. (2022). The response of gas hydrates to tectonic uplift. *Transport in Porous Media*, *144*(3), 739-758.

Oyama, A., & Masutani, S. M. (2017). A review of the methane hydrate program in Japan. *Energies*, *10*(10), 1447.

Pang, W., Chen, M., Fu, Q., Ge, Y., Zhang, X., Wen, H., ... & Li, Q. (2024). A Comparative Study of Hydrate-Based CO2 Sequestration at Different Scales. *Energy & Fuels*.

Phillips, S. L., Igbene, A., Fair, J. A., Ozbek, H., & Tavana, M. (1981). A technical databook for geothermal energy utilization.

Rehman, A. N., Bavoh, C. B., Pendyala, R., & Lal, B. (2021). Research advances, maturation, and challenges of hydrate-based CO2 sequestration in porous media. *ACS Sustainable Chemistry & Engineering*, *9*(45), 15075-15108.

Reid, R. C., Prausnitz, J. M., & Poling, B. E. (1987). The properties of gases and liquids.

Ruppel, C. D., & Kessler, J. D. (2017). The interaction of climate change and methane hydrates. *Reviews of Geophysics*, *55*(1), 126-168.

Singh, R. P., Lall, D., & Vishal, V. (2022). Prospects and challenges in unlocking natural-gas-hydrate energy in India: Recent advancements. *Marine and Petroleum Geology*, *135*, 105397.

Snæbjörnsdóttir, S. Ó., Sigfússon, B., Marieni, C., Goldberg, D., Gislason, S. R., & Oelkers, E. H. (2020). Carbon dioxide storage through mineral carbonation. *Nature Reviews Earth & Environment*, *1*(2), 90-102.

Span, R., & Wagner, W. (1996). A new equation of state for carbon dioxide covering the fluid region from the triple-point temperature to 1100 K at pressures up to 800 MPa. *Journal of physical and chemical reference data*, *25*(6), 1509-1596.

Spycher, N., & Pruess, K. (2010). A phase-partitioning model for CO 2–brine mixtures at elevated temperatures and pressures: application to CO 2-enhanced geothermal systems. *Transport in porous media*, *82*, 173-196.

Sullivan, M., Rodosta, T., Mahajan, K., & Damiani, D. (2020). An overview of the Department of Energy's CarbonSAFE Initiative: Moving CCUS toward commercialization. *AIChE Journal*, *66*(4), e16855.

Tohidi, B., Yang, J., Salehabadi, M., Anderson, R., & Chapoy, A. (2010). CO2 hydrates could provide secondary safety factor in subsurface sequestration of CO2. *Environmental science & technology*, *44*(4), 1509-1514.

Verma, A., & Pruess, K. (1988). Thermohydrological conditions and silica redistribution near high-level nuclear wastes emplaced in saturated geological formations. *Journal of Geophysical Research: Solid Earth*, *93*(B2), 1159-1173.

Wagner, W., & Kretzschmar, H. J. (2008). IAPWS industrial formulation 1997 for the thermodynamic properties of water and steam. *International steam tables: properties of water and steam based on the industrial formulation IAPWS-IF97*, 7-150.

White, M. D., Bacon, D. H., White, S. K., & Zhang, Z. F. (2013). Fully coupled well models for fluid injection and production. *Energy Procedia*, *37*, 3960-3970.

White, M. D., Kneafsey, T. J., Seol, Y., Waite, W. F., Uchida, S., Lin, J. S., ... & Zyrianova, M. (2020). An international code comparison study on coupled thermal, hydrologic and geomechanical processes of natural gas hydrate-bearing sediments. *Marine and Petroleum Geology*, *120*, 104566.

You, K., & Flemings, P. B. (2018). Methane hydrate formation in thick sandstones by free gas flow. *Journal of Geophysical Research: Solid Earth*, *123*(6), 4582-4600.

Zander, T., Choi, J. C., Vanneste, M., Berndt, C., Dannowski, A., Carlton, B., & Bialas, J. (2018). Potential impacts of gas hydrate exploitation on slope stability in the Danube deep-sea fan, Black Sea. *Marine and Petroleum Geology*, *92*, 1056-1068.